Materials Science & Engineering A 912 (2024) 146948

Contents lists available at ScienceDirect

Materials Science & Engineering A

journal homepage: www.elsevier.com/locate/msea

Effect of sigma phase on CVN impact toughness in HDSS weld metal

Andres Acuna [a,b,*], Kaue Correa Riffel [b,c], Antonio Ramirez [b,**]

[a] Lincoln Electric Cleveland, OH, USA
[b] Ohio State University Columbus, OH, USA
[c] Universidade Federal de Santa Catarina Florianópolis, SC, Brazil

ARTICLE INFO

Keywords:
Phase transformation
Precipitation
Duplex stainless steel
Intermetallic
Ductility
Cryogenic
Kinetics

ABSTRACT

This work uses kinetics calculation and a thermomechanical physical simulator to evaluate the sigma phase precipitation in Hyper Duplex Stainless Steel (HDSS) as-welded microstructure for impact toughness evaluation. Precipitation bars were machined out of a HDSS deposited clad mockup and submitted through aging on the thermomechanical physical simulator. Bars with sigma phase volumes of 0 %, 0.16 %, 0.52 %, 0.9 % and 4.3 % were created and machined to sub-size CVN specimens. Through impact CVN testing, complete ductile-to-brittle-transition-temperature (DBTT) curves were developed based on absorbed energy (kV), lateral expansion (LE), and shear fracture appearance (SFA) criteria for each sigma phase volume. It was seen that sigma phase presence provides drastic reduction on toughness the HDSS. The DBTT increased from −52.29°C to 38.32°C while the upper shelf energy (USE) is reduced from 68.85J to 11.66J with the increase sigma phase volume. Both the DBTT and USE presented a behavior well fitted through a sigmoidal curve. While very low sigma phase volumes caused little change on the DBTT and USE values, a saturation effect could be inferred on the USE at 4.3 % vol of sigma phase. CVN samples' secondary cracks high-resolution images suggest that the ferrite and austenite arrest crack propagation while the brittle sigma grains, depending on size and orientation propagate the cracks.

1. Introduction

Duplex Stainless Steels (DSS) are named after the duplex microstructure containing about 50 % ferrite and 50 % austenite. This configuration results in great corrosion resistance, coupled with good toughness and yield strength, thus facilitating widespread use across various industries [1].

The mixed microstructure confers toughness higher than ferritic stainless steels but slightly lower than purely austenitic stainless steels. In these materials, austenite's FCC structure predominantly governs toughness performance due to its greater abundance of slipping planes. While most FCC materials do not exhibit a pronounced temperature-dependent Ductile-to-Brittle-Transition-Temperature (DBTT) curve, high-nitrogen FCC austenitic stainless steels show a significant DBTT curve [2].

Over the last decade, duplex stainless steels have seen an increase in typical nitrogen content as manufacturers rely more on the nitrogen role for austenite stabilization. The recently developed Hyper Duplex Stainless Steel (HDSS) boasts a high alloying content, including 0.4%wt. Nitrogen, surpassing a pitting resistance equivalent number PREn of 48 [3–5]. Furthermore, it exhibits a unique propensity to form high austenite volumes upon welding. Acuna et al. [6,7] have demonstrated through thermodynamic calculations the nitrogen role in stabilizing austenite in HDSS welds. The austenite stable field can be significantly shrunk when the content changes from 0.2%wt. To 0.4%wt. For this reason, the authors also presented that the nitrogen content in the shielding gas of HDSS welding is important to mitigate losses of this element during the process.

However, the high chromium and molybdenum in this alloy could exacerbate susceptibility to sigma phase formation. Sigma phase, the most prominent intermetallic to occur at higher temperatures (600 °C–1000 °C), grows into the ferrite phase, depleting chromium and molybdenum and consequently reducing corrosion resistance [1,8,9].

The sigma phase is very hard and brittle, with the original report from Bain and Griffiths [10] reporting hardness of approximately 68 Rockwell C, and the brittleness was attributed because the samples were often fractured while testing. Marcinkowski and Miller [11] related the brittleness of the sigma phase, in the Fe–Cr system, at room temperature to the difficulty of dislocation generation in such a partially ordered lattice, relating the high temperatures ductility to a less ordered structure, which suggested a possibility of an order-disorder transition in

* Corresponding author.
** Correponding author. Department of Materials Science and Engineering, 1248 Arthur E. Adams Drive, Columbus, OH, 43221, USA.
E-mail addresses: acuna.43@osu.edu, andres_acuna@lincolnelectric.com (A. Acuna), ramirez.49@osu.edu (A. Ramirez).

https://doi.org/10.1016/j.msea.2024.146948
Received 26 April 2024; Received in revised form 15 June 2024; Accepted 11 July 2024
Available online 14 July 2024

Symbol list

PREn	Pitting Resistance Equivalent Number
DSS	Duplex Stainless Steel
SDSS	Super Duplex Stainless Steel (40<PREn>48)
HDSS	Hyper Duplex Stainless Steel (PREn>48)
α	Ferrite phase
DBTT	Ductile-to-Brittle-Transition-Temperature
USE	Upper Shelf Energy
kV	Absorbed Energy
LE	Lateral Expansion
SFA	Shear Fracture Appearance
FCC	Face centered cubic
γ	Austenite phase
γ_2	Secondary austenite phase
σ	Sigma phase
SEM	Scanning Electron Microscopy
EBSD	Electron Backscattered Diffraction
FS CVN	Full size CVN specimen (10 mm × 10 mm x 55 mm as per ASTM E23)
SS CVN	Subsize CVN specimen (10 mm × 5 mm x 55 mm as per ASTM E23)

sigma phase. More evidence was found in the works of Mima and Imoto [12] and Bungardt and Spyra [13], where "changes" in the sigma phase suggested different Young's Modulus at high and room temperature.

Therefore, the sigma phase presence hampers mechanical properties, with severe impact toughness reduction due to the difficulty of dislocation generation and the low dislocation mobility within the sigma phase's tetragonal partially ordered structure [8,11,14,15]. Severe impact toughness reduction was seen once the sigma phase is formed [8,11,16–19].

The Charpy V-Notch test provides a simple and rapid means of evaluating impact toughness. Lucon et al. [15] have extensively utilized this technique for comparing material toughness performance. As per ASTM E23 [14], the absorbed energy is derived from a pendulum striker's impact on a V-notched bar specimen, with additional evaluation criteria Lateral Expansion (LE) and Shear Fracture Appearance (SFA) evaluated from the tested specimen.

While the concept of sigma phase toughness reduction is known, the quantification of this reduction remains inadequately explored. Some research has been developed on the toughness reduction of DSS [9,19–24] and SDSS [16–18,24–26].

Breda et al. [18] compared the impact fracture toughness of super duplex stainless steel plates in wrought and aged conditions (0.5 % intermetallics volume – sigma and chi phases), observing a significant decrease in Upper Shelf Energy (USE) and an increase in DBTT. However, due to the simultaneous presence of sigma and chi phases, it was challenging to isolate the effect of each phase on impact toughness.

Similarly, Calliari et al. [17] investigated the effect on intermetallic formed on the range 800 °C–950 °C on 2205 duplex stainless steel. In this alloy, it was found that fine disperse volume smaller than 0.5 % intermetallics (at this volume only chi phase is present) caused a degree of impact energy reduction, however, with a completely ductile fracture behavior. At intermetallics volumes higher than 1 % (chi and sigma phase were present) brittle fracture behavior was found. Interestingly, when analyzing a higher alloyed material (SDSS) Calliari et al. [16] an impact toughness reduction of 50 % once only 0.5 % intermetallics volume was present. Once again, the chi and sigma phase are present, and the effect of sigma phase separately could not be considered.

However, on the HDSS, as a new material, with higher austenitic volume and its specific sigma phase kinetics [6,7,27–30], there's a lack of understanding regarding the relevance of sigma phase presence on toughness. Nevertheless, little effort has been put into evaluating this material toughness performance, and even less into considering impact toughness reduction as a function of sigma phase volume. Most of the research developed in HDSS evaluated the material's corrosion performance when the sigma phase is present [31–48].

Therefore, this study builds on previous research on sigma phase kinetics model for highly alloyed duplex stainless steels [6,7,27,30] to artificially induce controlled amounts of sigma phase in the weld metal. Differently from what has been published [16–19], this work developed full DBTT curves using three criteria, absorbed energy (kV), lateral expansion (LE), and surface fracture appearance (SFA) for six sigma phase volume fractions. Beyond only reporting the impact toughness reduction as a function of sigma phase volume, this research fitted sigmoidal regressions developing sigma phase volume dependent correlations for the DBTT behavior and another for the USE ductility.

2. Materials and methods

2.1. Materials

Fig. 1 presents the source and configuration of both materials. The as-welded precipitation bars specimens (70 mm × 10 mm x 5 mm) were machined from a three-layered cladded mockup presented in Fig. 1 (c). Chemical composition of base material is available in Supplementary Material Table S1. Machining of the specimen aimed to encompass the microstructures of all three layers, focusing on the second layer's center. The specimens were machined from different locations, discarding 25 mm of material from the start and end regions of the welding beads, as shown in Fig. 1 (b). Two cladded mockups were produced with automated GTAW process with distinct heat inputs (1.65 kJ/mm and 2.00 kJ/mm), interpass temperature controlled at 100 °C and 200 °C, and a 27.7.5.L HDSS filler metal with 1.2 mm in diameter. Welding parameters are provided in the Supplementary Material Table S2.

Table 1 presents the material's chemical composition measured through Optical Emission Spectroscopy (OES) on the precipitation bars cross-section. Since the emission line of nitrogen is in the region of extremely short wavelengths for OES, its amount was also validated using a combustion spectrometer Leco TC600.

The specimen's machining aimed for precise centering on the second layer, encompassing the entire microstructure of this layer, along with 1.25 mm from the first layer and an additional 1.25 mm from the third layer.

2.2. Experimental procedure

2.2.1. Sigma phase precipitation experiment

The material's evaluation was conducted on as-welded microstructure, initially free of any intermetallic presence. Specific heat treatments deliberately induced sigma phase precipitation. The procedure for artificially inducing precipitation was as follows:

The Gleeble® physical simulator was utilized to subject the material to a specific thermal cycle. This cycle entailed a heating rate of 100 °C/s, starting from room temperature and reaching a peak temperature of 1125 °C. The peak temperature was maintained for a duration of 0.5 s. Subsequently, controlled cooling was initiated, with a constant cooling rate employed to attain a predefined sigma phase volume fraction. This approach was developed using the previous sigma phase kinetics model [30]. Details of the precipitation procedure are provided in the supplementary material.

Intermetallic volume fractions were quantified using quantitative electron microscopy on a FEI Apreo LoVac High Resolution. The sample preparation involved grinding from 240 to 1200 grit, followed by diamond paste polishing (1 μm), and a final 0.02 μm colloidal silica polishing for 3 h. Microstructural etching was performed using a modified version of Ramirez et al. [49] dual-step electrolytic etching process. This process involved a 40 % HNO_3 + 60 % distilled water solution for

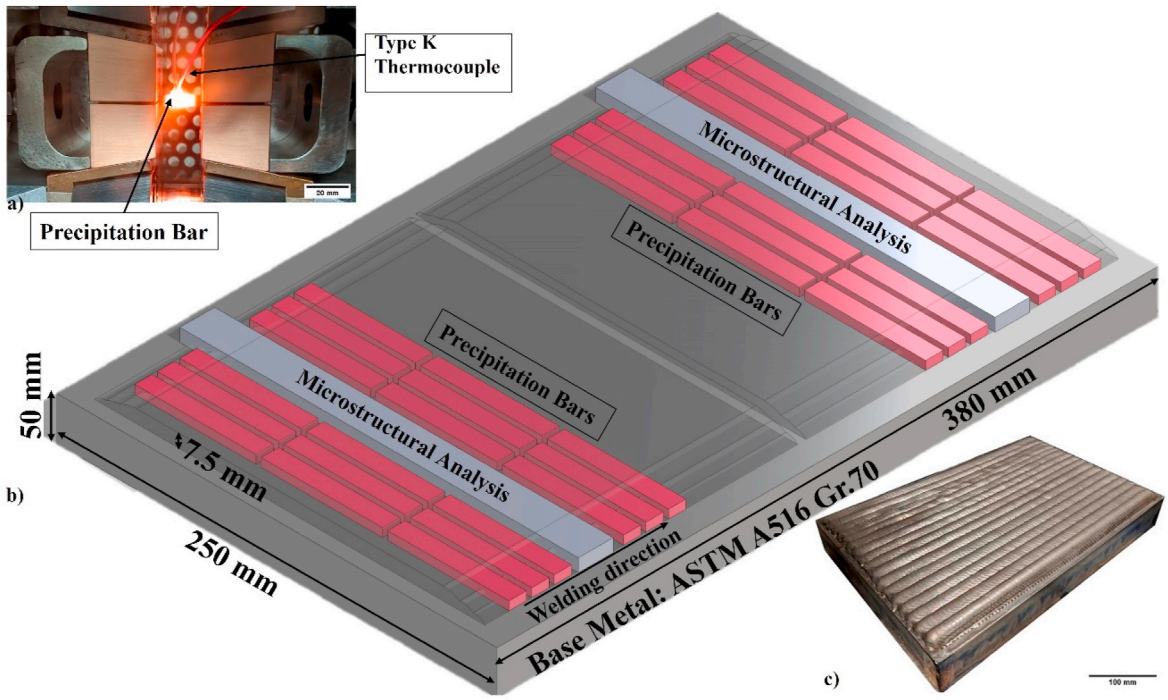

Fig. 1. -Materials specimen. (a) precipitation experiment on the Gleeble. (b) schematic of specimen location of the precipitation bars in red and microstructural analysis specimen in grey. (c) cladded mockup from which the "as-welded" specimens were machined. (For interpretation of the references to color in this figure legend, the reader is referred to the Web version of this article.)

Table 1
OES Measured chemical composition in wt.% on the precipitation bar samples used in physical simulation.

Material	Fe	C	Cr	Ni	Mo	N	Co	Mn	PREn
HDSS weld metal	Bal.	0.023	26.05	6.31	4.74	0.40	1.32	0.96	48.0

interphase etching, with a first step of 1.3V for 20 s, followed by 0.9V for 60–240 s for ferrite preferential etching. The quantifying phase fractions procedure by digital image analysis and thresholding grayscale images from SEM is described in detail in previous works [6,7,27,30].

Two mockups M1.6IT100 and M2IT200 were used for the experiments due to the following reasons:

- Both mockup conditions yielded nearly identical sigma phase-free DBTT curves, with similar DBTT and USE values.
- Both mockup conditions exhibited closely matched volume distributions of austenite and ferrite phases, particularly at the second layer, which represents the primary microstructure of the utilized impact specimen.
- The primary limitation on impact toughness arises from the volumetric fraction of the sigma phase.
- The availability of specimens was constrained.

The experiment conditions, corresponding specimen set name, cooling rates and the resultant sigma phase volumes can be found in Table 2. The heat treatment temperature is controlled by a feedback type-K thermocouple positioned at the center of the specimen.

Consequently, the analysis of results centers on the volumetric effect of the sigma phase rather than the specific mockup conditions. Nonetheless, the figures and tables presented continue to specify the mockup condition employed.

After the sigma phase precipitation cycle, the Charpy notch was strategically positioned precisely within the region where the cooling rate had been controlled. Ultimately, the sample was trimmed to achieve a final subsize length of 55 mm [14].

Table 2
HDSS impact test condition and sigma phase volume fraction as a function of the cooling rate.

Weld Condition	Mockup name	Cooling rate [°C/s]	Sigma [% vol]	Standard Error[a]
1.65 kJ/mm IT 100 °C	M1.6IT100	>20	0	N/A
2.0 kJ/mm IT 200 °C	M2IT200	>20	0	N/A
2.0 kJ/mm IT 200 °C	M2IT200	2.5	0.16	±0.04
2.0 kJ/mm IT 200 °C	M2IT200	1.3	0.52	±0.10
2.0 kJ/mm IT 200 °C	M2IT200	1.0	0.90	±0.14
1.65 kJ/mm IT 100 °C	M1.6IT100	0.9	4.3	±0.75

[a] Standard Error calculated for a 95 % confidence interval.

2.2.2. *Subsize DBTT curve development*

The construction of the Ductile-to-Brittle-Transition-Temperature (DBTT) curves for the HDSS as-welded material relied on impact toughness measurements. Utilization of a Tinius Olsen model-64 impact tester featuring a 540 J pendulum was critical. The testing procedure and specimen dimensions closely adhered to the guidelines outlined in standard ASTM E23 [14].

Notably, each specimen was fitted with a type-T thermocouple, 0.254 mm diameter, positioned proximate to the notch area. This thermocouple served the purpose of recording the specimen's temperature at the moment of pendulum impact. To establish uniformity in

testing conditions, the specimens were subjected to 1 min of immersion in liquid nitrogen, effectively stabilizing the temperature at −196 °C. Subsequently, the specimens were situated on the equipment anvils until the attainment of the designated testing temperature.

Owing to the constraint imposed by the maximal cladding layer thickness of approximately 7.5 mm, it was necessary to utilize subsize specimens. Therefore, the subsize CVN specimen were centered on the second deposited layer, which presented higher uniformity between both cladding conditions. Based on ASTM E23 [14], the subsize specimen 2B (10 mm × 5 mm X 55 mm). In this context, the reduction in size by half, solely pertained to the thickness dimension (denoted as "B" in the standard), as depicted in Fig. 2. Notably, the striking direction, notch depth, notch radius, and crack propagation length were preserved in congruence with the specifications for the full-size specimen.

The DBTT curves were determined through the utilization of the hyperbolic tangent equation (Equation (1)), with parameters T_o and C being defined through the solution of least squares calculations, in accordance with the method delineated by Lucon et al. [15,50].

$$Y = A + B\,tanh\frac{T - T_o}{C} \quad (1)$$

Where, A is the average value between the Upper Shelf Energy (USE) and the Lower Shelf Energy (LSE); B represents the difference between the USE value and A; C is half of the temperature transition range from the USE to LSE; and T_o corresponds to the DBTT value. The computation of the DBTT curves was conducted according to three specified criteria in the standard, which encompassed impact energy (kV), lateral expansion (LE), and surface fracture appearance (SFA) [14].

Furthermore, a regression analysis was constructed to elucidate the behavior of both DBTT and USE concerning the volume fraction of sigma phase. This was achieved by fitting the obtained results into a symmetric sigmoidal curve, facilitating an encompassing depiction of the relationship.

3. Results and discussion

3.1. Material and microstructure characterization

Fig. 3 illustrates the as-welded microstructure on the HDSS second layer cladding, which undergoes reheating solely by the third layer. Within this intermediate layer, the α→γ transformation is comparatively less extensive than the first layer, resulting in a microstructure balance that approximates the targeted 50 % distribution. Specifically, the M1.6IT100 condition yielded a ferrite volume fraction of 51.72 % ± 1.13 %, while the M2IT200 condition exhibited a similar ferrite content of 48.99 % ± 9.03.

The thermal history shows the second layer reheating cycle achieving a peak temperature exceeding 1500 °C, rapid Cr_2N dissolution occurs while nitrogen enrichment takes place in the ferrite. Subsequent rapid cooling, at approximately 90 °C/s, induces swift nitrogen supersaturation within the ferrite, leading to intense precipitation. Notably, intense Cr_2N precipitation, forming colonies inside the ferritic matrix, is marked by blue ellipses, Fig. 3.

Both welding conditions resulted in Cr_2N precipitation. Qualitatively, M1.6IT100 exhibited higher precipitation, attributed to the higher ferrite content, reduced heat input, and lower interpass temperature. Additionally, intragranular secondary austenite precipitation associated with chromium nitride is observed. In the examined images, the secondary austenite grain size in the higher heat input scenario (M2IT200) is qualitatively larger, a consequence of the higher peak temperature reached and lower cooling rates.

Fig. 4 presents a secondary electron SEM image from the M1.6IT100 s layer with Cr_2N presence. In this image, a triple junction is apparent between two ferrite grains and an austenite grain. The red arrow

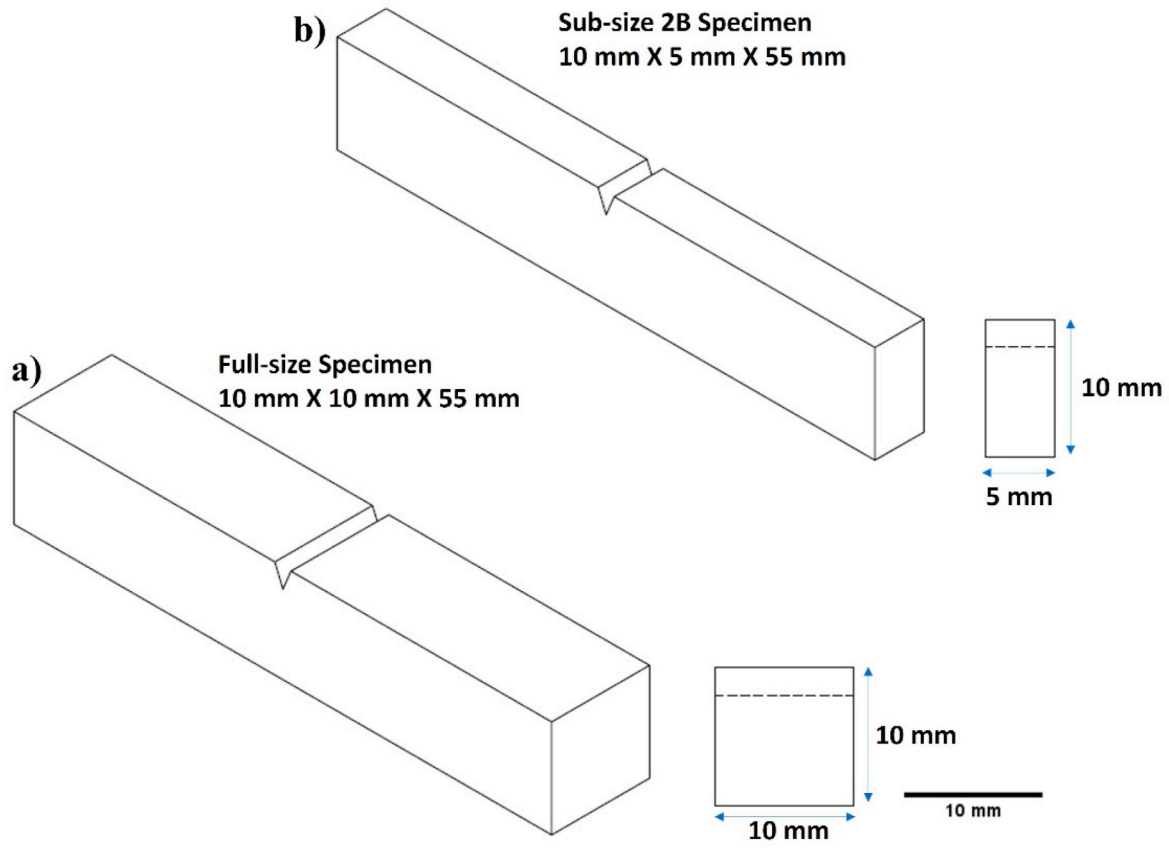

Fig. 2. Impact toughness Charpy V-notch specimen. Comparison of the standard full size and the subsize 2B used in this research as per ASTM E23 [14].

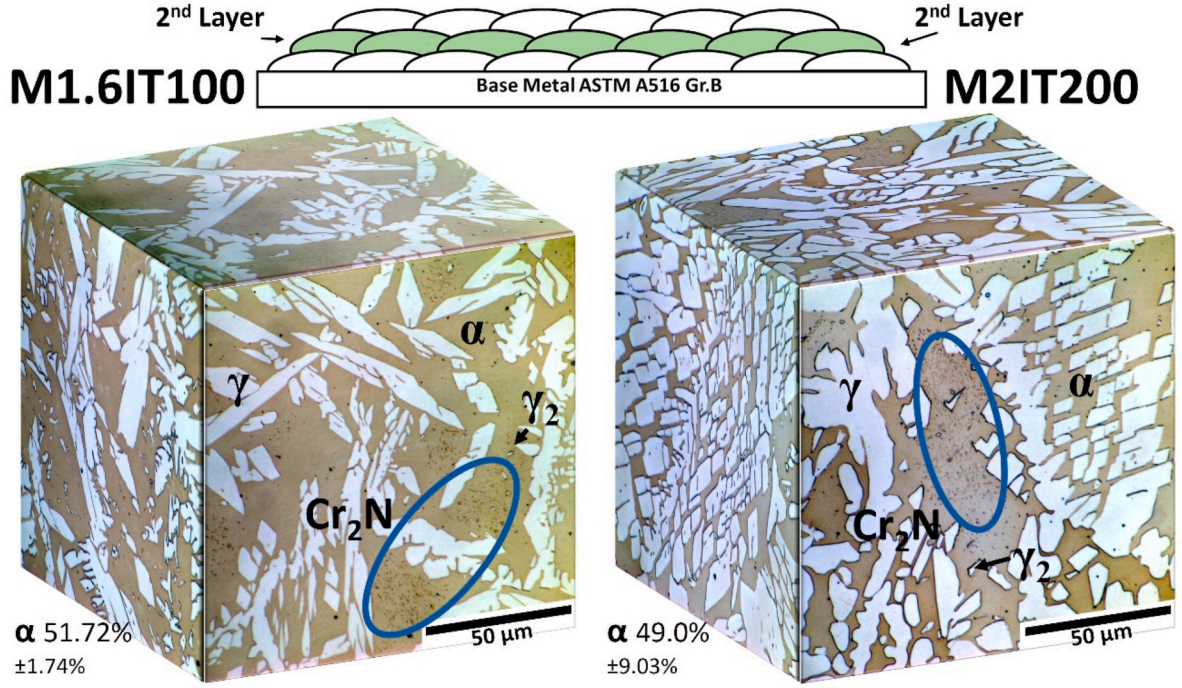

Fig. 3. Second layer cladded mockups 3D microstructure representation,. The less hot condition, M1.6IT100, is on the left, and the optimized heat input condition, M2IT200, is on the right. The blue ellipses mark intense Cr_2N precipitation creating colonies inside the ferritic matrix. (For interpretation of the references to color in this figure legend, the reader is referred to the Web version of this article.)

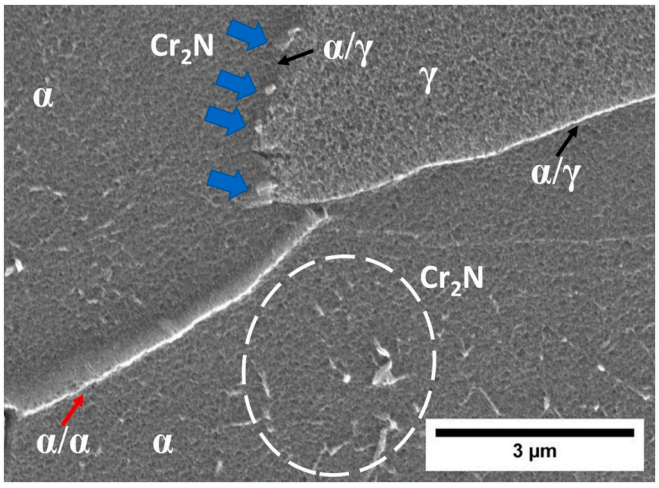

Fig. 4. Chromium nitride present on the M1.6IT100 mockup. Intragranular Cr2N within the ferritic matrix, white dashed ellipsis. Intergranular Cr2N (blue arrows) at the α/γ interface, black arrow and α/α grain boundary, red arrow. (For interpretation of the references to color in this figure legend, the reader is referred to the Web version of this article.)

signifies the α/α grain boundary, while the black arrows highlight the α/γ interfaces. In both ferrite grains, intragranular Cr_2N colonies are evident, delineated by white dashed lines. Furthermore, intergranular Cr_2N is observed at the upper α/γ interface. The interaction of Cr_2N with austenite is as anticipated, primarily following an orientation relationship where the most compact planes of ferrite, austenite, and Cr_2N are parallel, denoted as $(111)_\gamma||(110)_\alpha||(0001)_{Cr2N}$, as elucidated by Ramirez et al. [49,51]. This orientation relationship arises from the parallel orientation relationship of the most compact planes between ferrite and Cr_2N, also noted in intragranular precipitation, combined with the Kurdjumov-Sachs (K–S) orientation relationship at the α/γ interfaces.

No sigma phase was observed in the second layer microstructure. The sigma phase temperature range's, 1100 °C–700 °C, cooling rates were 22 °C/s. This agrees with the previous research from Acuna et al. [6,7,27], finding no sigma phase formation at cooling rates higher than 4 °C/s.

3.2. *Impact toughness - DBTT curves results*

Without sigma phase presence, both mockups, M1.6IT100 and M2IT200, presented equivalent DBTT curves, regardless the welding parameters. The graph in Fig. 5 displays the measured data as blue squares and green triangles, representing M1.6IT100 and M2IT200, respectively. Corresponding DBTT curves followed suit with color

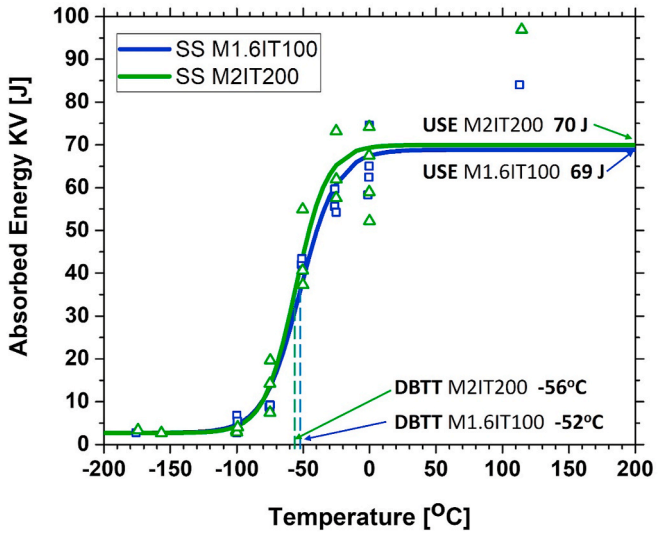

Fig. 5. Sub-size CVN DBTT curve in the as-welded condition. No intermetallic presence.

coding and were established through hyperbolic tangent function fitting. The calculated DBTT and USE values closely aligned between the two conditions, nearly equivalent at −52 °C, 69J for M1.6IT100, and -56 °C, 70J for M2IT200.

The small performance difference is attributed to the austenite volumetric fraction [8]. M2IT200 exhibited a slightly higher average austenite volume fraction (47.6 %) than M1.6IT100 (47.1 %), alongside an elevated presence of Cr_2N in M1.6IT100 resulting on the marginal reduction in DBTT and USE values for M1.6IT100.

Table 3 presents the results comparison of both heat input conditions. $FATT_{50}$ stands for fracture appearance transition temperature of fifty percent, a corresponding evaluation of the DBTT on the SFA curve. The table shows a high agreement of the M1.6IT100 DBTTs results in all criteria, with only the lateral expansion diverging about five degrees. Conversely, the M2IT200 DBTTs presented high agreement in the LE and $FATT_{50}$ values but differed slightly from the kV criteria. The absorbed energy (kV) is the most used criterion, with some standards such as the API RP582 [52] now also including the LE criteria as a recommendation. Lucon et al. [15] claimed that the three transition temperature definitions, $DBTT_{kV}$, $DBTT_{LE}$, and $FATT_{50}$, should agree within ±25 °C. In this research, all transition criteria agreed within ±10 °C.

Given the literature limited data available for HDSS DBTT behavior, particularly in relation to sigma phase presence, this research endeavors to establish meaningful correlations. Despite the absence of an established full-size (FS) to sub-size (SS) curve correlation for the entire DBTT curve, certain factors like normalized USE and specific correlations offer insight [15,53,54]. Lucon et al. [15] compared multiple published area normalizing factors using multiple sub-size specimens. He proposed a new factor based on the ratio of the nominal fracture volumes expressed as: Bd^2, where B is the sample reduced thickness and d is the ligament size (width discounted of the notch depth).

Assuming the same hyperbolic tangent behavior and exhaustion of the material's ductility in both full-size and sub-size at very low temperatures, *i.e.*, negligible changes of the lower shelf energy value. It is possible to calculate a DBTT curve to create data qualitatively comparable with the material's data sheet reference. This was established by fitting the hyperbolic tangent equation using the same measured LSE value, the DBTT correlated value (average of Towers' and Wallin's correlation) [53,54], the normalized USE value using Lucon's factor (NF8), and using the same temperature transition width measured, Fig. 6.

In Fig. 6, the continuous red line represents the material's full-size (FS) reference. Calculating from this data yields a DBTT of −54.2 °C, a USE of 261.7 J, and an LSE of 5.88 J. The close match between the full-size LSE and the measured sub-size LSE validates the assumption that complete ductility exhaustion occurs at extremely low temperatures, approximately −180 °C. The previously observed sub-size DBTT curves from Fig. 5, are displayed in solid blue and green lines, while qualitatively correlated DBTT curves are shown in dashed lines, following the color pattern of M1.6IT100 in blue and M2IT200 in green.

It is critical to consider that the HDSS normalized (NF8) USE values lower than the results reported for wrought 2205 DSS [17] and SDSS [16] materials without sigma phase presence. This reduction is due to the role of welding, the as-welded microstructure has inherently lower toughness when compared to the wrought material, as the phase distribution and phase morphology are severely distinct and also play role in the sigma phase's formation kinetics [30,55].

While these curves are plotted for qualitative comparison, the DBTT and USE values are calculated using validated correlations, allowing for a valid quantitative comparison. The fully correlated DBTT is −33.70 °C and −37.14 °C for M1.6IT100 and M2IT200, respectively, representing an increase of around 18.5 °C after welding. Similarly, the fully correlated USE is 168.85 J for M1.6IT100 and 172.60 J for M2IT200, showing a reduction of approximately 90.5 J after welding. Notably, the as-welded microstructure's impact toughness data is not as optimal as that of the forged material. This difference stems from processing conditions, as the forged material exhibits distinct microstructure, grain texture, and higher stored deformation that collectively influence toughness performance. Despite these disparities, these are the novel as-welded HDSS DBTT curves, rendering this material data valid across specimen sizes.

Table 3
Cladded condition comparison of the maximum toughness and temperature transition results.

Welding Condition	$DBTT_{kV}$ [°C]	$DBTT_{LE}$ [°C]	$FATT_{50}$ [°C]	USE [J]
M1.6IT100	−52.29	−47.83	−52.92	68.85
M2IT200	−55.74	−62.57	−64.62	69.97

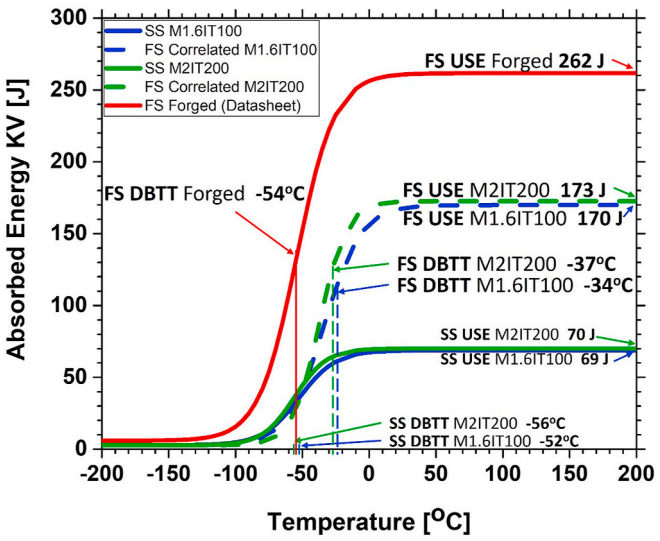

Fig. 6. DBTT curve correlation chart. The red line presents the full-size (FS) CVN specimen forged microstructure. The subsize (SS) CVN specimen are presented by the continuous green and blue lines. The fitted full-size curves, using separated correlations for the DBTT and for the USE, are presented in the dashed green and blue lines. (For interpretation of the references to color in this figure legend, the reader is referred to the Web version of this article.)

The presence of the sigma phase can lead to a significant reduction in impact toughness presence [8,16–18]. This reduction is attributed to the tetragonal, partially ordered structure of the sigma phase, characterized by low dislocation mobility [1,11,56–59]. While the HDSS investigated in this study has demonstrated resistance to sigma phase precipitation during welding [6,7,30], it remains crucial for the industry and scientific community to evaluate how the presence of the sigma phase impacts impact toughness.

Given the impossibility of naturally inducing sigma phase presence during welding [6,7,30], sigma phase formation was artificially induced using a Gleeble® physical simulator applied to the as-welded microstructure [30]. The summarized results and correlations, including DBTT and USE correlations based on the work of Towers et al. [53] and Wallin et al. [54], as well as USE area normalizing factor (NF8) based on Lucon et al. [15], are presented in Table 4. These correlations are applicable to both mockups and all sigma phase volume fractions assessed.

Table 4 offers a comprehensive summary of impact toughness CVN subsize results, presenting data for various sigma phase volume fractions: 0 % vol on M1.6IT100, 0 % vol on M2IT200, 0.16 % vol on M2IT200, 0.52 % vol on M2IT200, 0.9 % vol on M2IT200, and 4.3 % vol on M1.6IT100.

The consensus that sigma phase presence reduces toughness is confirmed and agrees with previous works [16–18]. However, only understanding the general impact toughness (USE) as a function of intermetallic presence does not provides a complete analysis. The

Table 4
Impact toughness CVN subsize results summary for different iduced sigma fractions in the as-welded HDSS weld metal.

Sigma phase volume phase fraction	Measured Values				Towers et al. [53] correlation			Wallin et al. [54] correlation			Lucon et al. [15] Correlation
	$DBTT_{kV}$ [°C]	$DBTT_{LE}$ [°C]	$FATT_{50}$ [°C]	USE [J]	$DBTT_{kV}$ [°C]	$DBTT_{LE}$ [°C]	$FATT_{50}$ [°C]	$DBTT_{kV}$ [°C]	$DBTT_{LE}$ [°C]	$FATT_{50}$ [°C]	USE NF8 [J]
0 % vol on M1.6IT100	−52.3	−47.8	−52.9	68.9	−34.8	−30.3	−35.4	−32.6	−28.1	−33.2	169.8
0 % vol on M2IT200	−55.7	−62.6	−64.6	70.0	−38.2	−45.1	−47.1	−36.0	−42.9	−44.9	172.6
0.16 % vol on M2IT200	−50.3	−44.4	−55.9	66.9	−32.8	−26.9	−38.4	−30.6	−24.7	−36.2	165.0
0.52 % vol on M2IT200	−29.6	−26.8	−37.9	30.6	−12.1	−9.3	−20.4	−10.0	−7.1	−18.2	75.5
0.9 % vol on M2IT200	−24.1	−15.2	−19.2	16.7	−6.6	2.3	−1.7	−4.4	4.5	0.5	41.3
4.3 % vol on M1.6IT100	−8.3	−4.1	−6.5	11.7	9.2	13.4	11.0	11.4	15.6	13.2	28.8

kinetics analysis shown that the HDSS high alloy content show primarily sigma phase formation and very seldom chi phase appearance [7,30]. This characteristic provides the opportunity to understand the effect of sigma phase separately from chi phase, which is distinct and unique from the previous works. In addition, there is a critical demand from industry to understand how the impact toughness is reduced with the decrease of temperature. Hence, the novelty on the development of the entire DBTT curves for each sigma phase volume produced.

In Fig. 7, displays the calculated DBTT curves corresponding to the tested sigma phase volumes, including 0 % (both mockups), 0.16 %, 0.52 %, 0.90 %, and 4.3 %. A noticeable trend emerges as the DBTT increases with higher sigma phase volume. A greater sigma phase volume fraction renders the HDSS brittle at elevated temperatures. This effect is particularly pronounced when considering that a mere 0.52 % sigma phase volume leads to a DBTT shift of approximately 30 °C. More critically, at 4.3 % sigma phase volume, the DBTT increases by 46 °C, resulting in a DBTT as high as −8 °C. This temperature is easily attainable due to environmental fluctuations, especially in industrial settings such as oil and gas facilities.

An essential indicator of impact toughness is the upper shelf energy (USE), which quantifies the material's energy absorption capacity at its maximum ductility. A reduction in USE reflects a decrease in overall toughness. Fig. 7 visually demonstrates a progressive decrease in USE as the sigma phase volume increases. Notably, a sigma phase volume fraction as low as 0.52 % leads to a substantial 55 % reduction in USE. Moreover, sigma phase volume fractions of 0.90 % and 4.3 % result in even more pronounced reductions of 78 % and 82 % in USE, respectively.

It is possible to consider the HDSS USE results comparable with the results Previous research from Calliari et al. [16], in wrought Zeron®100 SDSS and on 2205 DSS [17] also with about 50 % of USE decrease at 0.5 % volume of intermetallics. Similar reduction seen on this research. However, while the previous research accounted for concomitant chi and sigma phase on wrought condition, our approach isolated sigma phase presence on as-welded HDSS microstructure.

Fig. 8 compares the three transition temperature definitions: $DBTT_{kV}$, $DBTT_{LE}$, and $FATT_{50}$, within a ±10 °C range. The specimens at 0.16 % and 0.52 % sigma phase exhibit higher scattering. Specifically, at 0.16 %, similar scattering is observed for $DBTT_{LE}$ and $FATT_{50}$, whereas at 0.52 %, $FATT_{50}$ deviates by almost 6 °C from $DBTT_{kV}$. Despite the DBTT results' scattering, all three criteria marked DBTT values within ±10 °C which is higher than the 25 °C defined by Lucon et al. [15].

Both material properties, DBTT and USE, display sigma phase volume fraction-dependent behavior. This relationship appears less sensitive at very low volumes, suggesting an asymptotic trend [16–18]. However, it becomes more sigma phase-dependent up to 0.90 %. Beyond this point, the dependence diminishes again, possibly indicating another asymptote.

The interaction between the sigma phase volume and the DBTT and

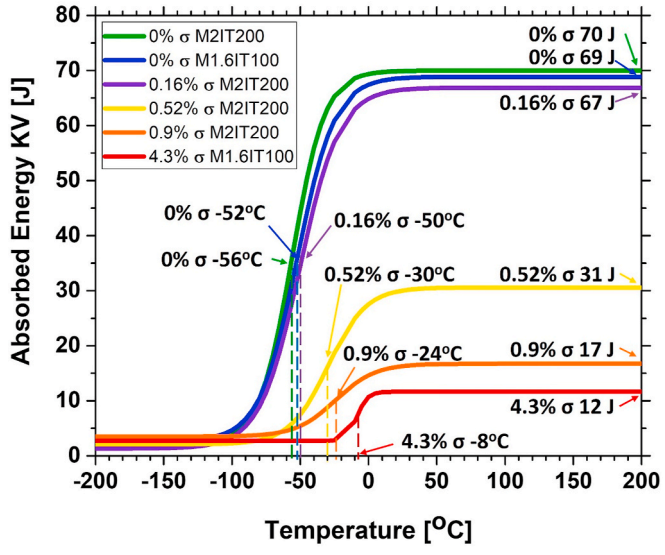

Fig. 7. As-welded HDSS DBTT curves for multiple sigma phase volumetric fractions.

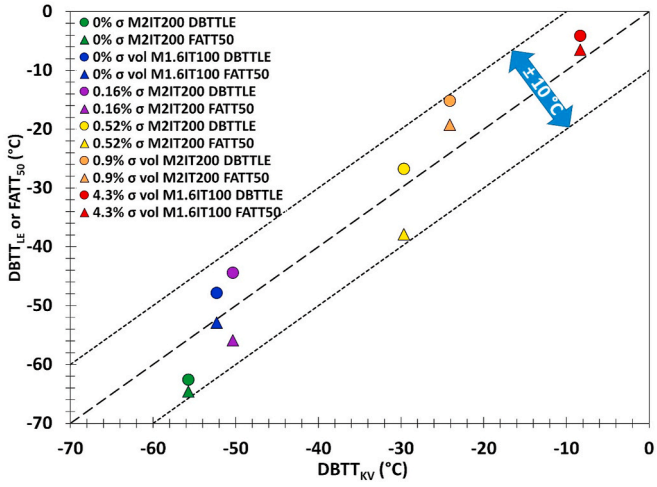

Fig. 8. HDSS Transition temperature comparison chart. Absorbed criteria (kV) is linked to the horizontal axis. The lateral expansion (LE) and the fracture appearance transition temperature of fifty percent ($FATT_{50}$) are presented in circular and triangular symbols. The farther the symbols are from the dashed diagonal, the higher the divergence from the $DBTT_{kV}$.

USE suggests a sigmoidal relationship. Fitting the data using the four-parameter logistics (4 PL) symmetric sigmodal regression produces a high agreement with the data with an R^2 of 0.988 for the DBTT fitting and 0.999 for the USE fitting. Table 5 presents the $DBTT_{kV}$ and USE values as a function of the sigma phase volume fraction and the corresponding 4 PL regression, visualized in Fig. 9 (a) and (b). It is critical to consider that each sigma phase volume, DBTT, and USE data set is extracted from the whole DBTT curve developed with 20 specimens, being a cost and time-consuming experiment. Due to the two conditions with 0 % sigma phase volume (1.65 and 2.0 kJ/mm), their average values of DBTT and USE were used in the regression for the upper shelf asymptote.

The DBTT regression suggests a sigma phase saturation effect beyond 4.3 % volume. Therefore, the DBTT value stabilizes around −7 °C. However, due to the limited available data sets, extrapolations for sigma phase volumes higher than 10 % might not be accurate. Accordingly, the USE regression suggests the saturation effect revealing an asymptotic behavior from 0.90 % to 4.3 % volumes of sigma phase to 12 J. This observed trend is expected since even with higher sigma phases volumetric fractions. There is always some amount of austenite to be cracked. The though austenitic phase produces a minimum energy absorption.

The results seen in DBTT and USE revealed that the material's toughness is already severely reduced at 4.3 % sigma phase volume. Higher sigma phase volumes are not feasible for real applications in the industry. In fact, the reduction of toughness measured at 0.52 % sigma phase volumes is likely a limitation to be recommended to standards. Interestingly, this high reduction of USE results at about 0.5 % of intermetallics volume was also seen in DSS [17] and in SDSS [16,18] all on wrought condition. However, besides the material's chemical composition, in the previous research chi phase and sigma phase precipitation overlapped and at lower volumes chi phase was predominant. The particular HDSS' chemical composition and the kinetics analysis developed on previously [6,7,27,30], made possible to develop specimen only with sigma phase presence. Therefore, allowing to understand the role solely of sigma phase into toughness. In special, the validity of this analysis is not only to assess the HDSS material's toughness. Instead, it is to establish a correlation for the material's toughness performance as a function of the sigma phase volumetric fraction.

Due to the specimen triaxiality, simultaneously with the main crack creating the fracture surface, secondary micro cracks are occurring inside the specimen, sometimes seen in the fracture surface, as shown in Fig. 10.

In Fig. 10, a specimen containing 0.16 % vol of sigma phase fractured at −74.5 °C reveals the initial fracture surface. On this surface, the machined notch appears on top, followed by dimples with some striation marks and small cleavage sections, as highlighted in the red box. Even at lower sigma phase volumes, these brittle regions were seen. Given the reduced sigma phase volume, these cleavage regions are highly related to the sigma phase presence, reduction of the crack-free path [18]. The highlighted brittle region is magnified in the image detail, revealing secondary cracks on the fracture surface.

To evaluate the secondary cracks, the CVN specimen was longitudinally sectioned in half, revealing an inner surface with apparent secondary cracks within 300 μm of the fracture surface, as shown in the schematic Fig. 11.

Table 5
Impact toughness subsize CVN measured and calculated regression results.

Condition	Sigma vol. [%]	$DBTT_{kV}$ [°C]	DBTT Regression [°C]	USE [J]	USE Regression [J]
M1.6IT100	0	−52.29	−54.85	68.85	69.72
M2IT200	0	−55.74	−54.85	69.97	69.72
M2IT200	0.16	−50.34	−48.53	66.87	66.50
M2IT200	0.5	−29.65	−32.31	30.59	30.85
M2IT200	0.9	−24.10	−21.88	16.74	16.16
M1.6IT100	4.3	−8.32	−8.85	11.66	12.04

The secondary crack analysis revealed an interesting effect; within a short range, approximately 300 μm, of the fracture surface, most of the sigma phase grains presented cracks, as is shown in Fig. 12, a specimen with 4.3 % of sigma phase broken at −5.7 °C. This results endorses the analysis of Breda et al. [18] and Calliari et al. [16,17] where the intermetallic precipitates cause cleavage and quasi-cleavages where the austenite and the ferrite matrix accumulate the plastic deformation energy.

A more detailed analysis using SEM secondary electrons combined with the backscattered signal, Fig. 13, revealed some key characteristics:

- The secondary cracks indicated the same direction of propagation from the main crack. *i.e.*, the crack direction followed the notch direction.
- The secondary cracks progressed mainly through the sigma phase while also propagating transgranular through the $\sigma+\gamma_2$ colonies, also breaking the thin secondary austenite lamellas.
- The cracks propagated through the sigma phase grain and were primarily arrested in the more ductile primary austenite grains, indicated by the blue arrows. This process created an extra half-circle deformation on the austenite interface [16–18], as shown in Fig. 13.
- Some cracks were also arrested in the ferrite grains, indicated by the red arrows.
- Multiple cracks were seen inside a single sigma phase grain.

Fig. 13 (d) revealed smaller and more straight cracks at the sample broken at −50 °C than in Fig. 13 (a, b, and c) broken at temperatures above +110 °C. In this condition, more deformation was seen on the austenite and ferrite grains. In addition, the crack opening was more significant at positive temperatures. Fig. 13 (a) and (c) show cracked $\sigma+\gamma_2$ colonies with crack propagation even though the secondary austenite. Even though the secondary austenite presents much higher ductility, these lamellas thinner than 1 μm could not deform enough to stop the crack.

Mao et al. [60] were able to link the secondary crack's average length with the specimen absorbed energy at the same temperature. In the studied alloy, he separated the crack lengths into short-range and long-range distributions, 0–15 μm and 15–30 μm, respectively.

In Fig. 14, a high-resolution SEM shows a detail of an etched specimen containing 4.3 % volume of sigma phase and broken at −5.7 °C, which resulted in an absorbed energy of 7.46 J, 0.06 mm of lateral expansion, and a shear fracture appearance of 10 %. The etching process primarily etched the sigma phase causing it to appear deeper on the image. In the image center, a transgranular crack created a flat facet surface across the sigma grain.

Interestingly, the region appearing as the crack center present a feature on the crack tip and at the interfaces with the surrounding austenite grains. On the top side of the crack, there is a small protrusion, marked by the red arrow, on the austenite grain. In contrast, on the opposite side, there is a small dent marked by the blue arrow. Because of the indications of the crack crossing the brittle sigma phase and stopping at the interface with the more ductile phases, as seen in Fig. 13, it is believed that this feature corresponds to a crack path, which starts at the red arrow and stops at the blue arrow. This feature is marked following the austenite interface inward of all the neighbors' grains suggesting the crack propagating also inward the figure plane along the sigma phase grain depth.

Depending on the microstructure alignment with crack propagation direction, the crack length can be significantly altered, as can be seen in Fig. 14 (c), with multiple small cracks crossing a thin (0.5 μm) sigma phase grain and a longer crack formed on a wider sigma phase grain section (6.7 μm).

The study of secondary cracks indicates that crack propagation depends on the sigma phase maximum grain size and orientation.

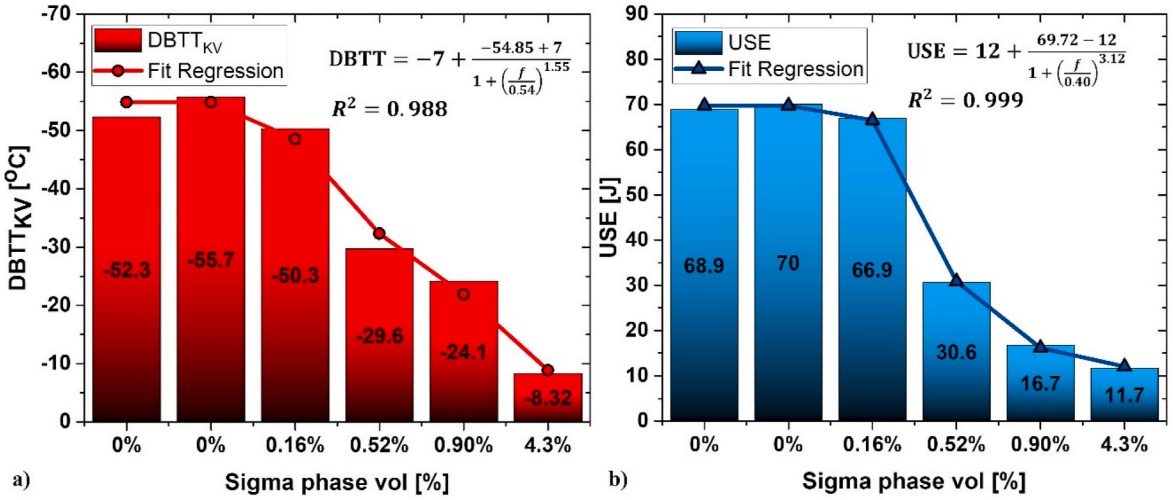

Fig. 9. Toughness fitted sigmoidal regressions. $DBTT_{kv}$ as a function of the sigma phase volume fraction in (a) and USE as a function of the sigma phase volume fraction in (b).

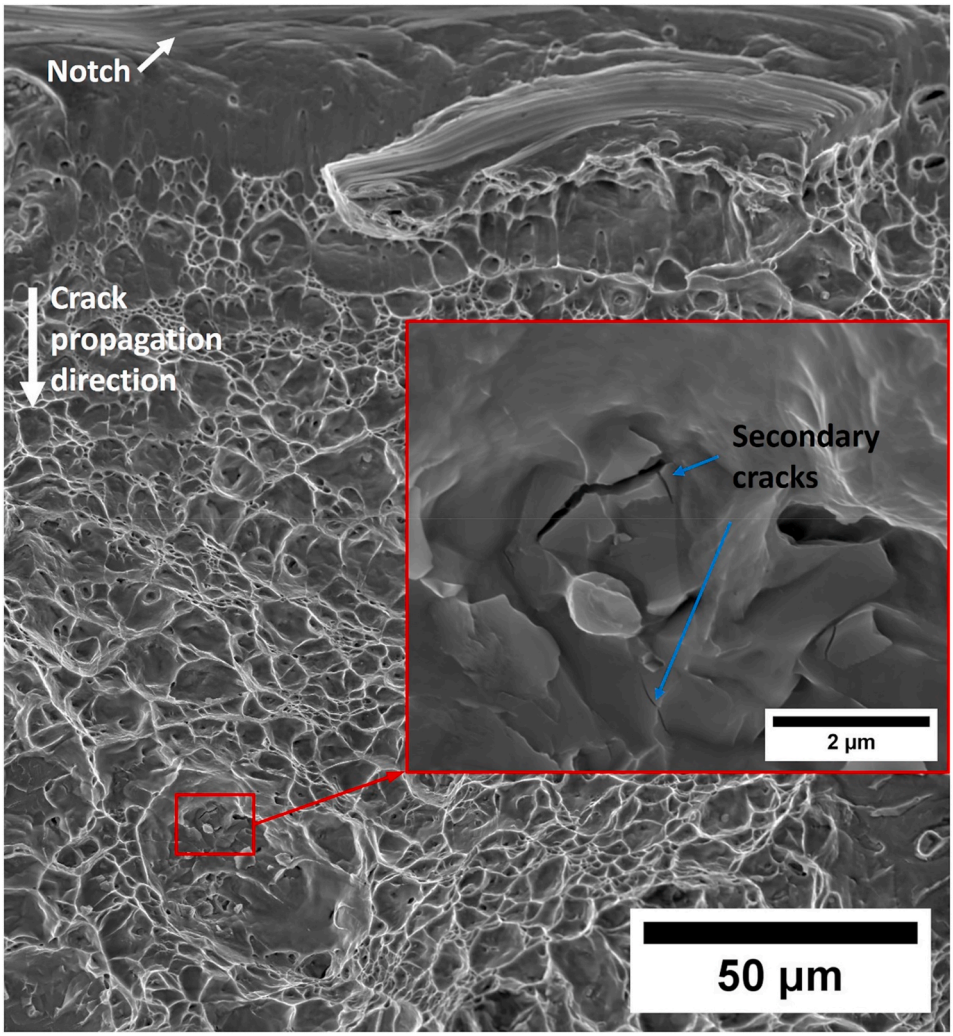

Fig. 10. Fractography of specimen containing 0.16 % vol of sigma phase fractured at −74.5 °C. The red box shows secondary cracks perpendicular to the primary notch crack propagation plane. (For interpretation of the references to color in this figure legend, the reader is referred to the Web version of this article.)

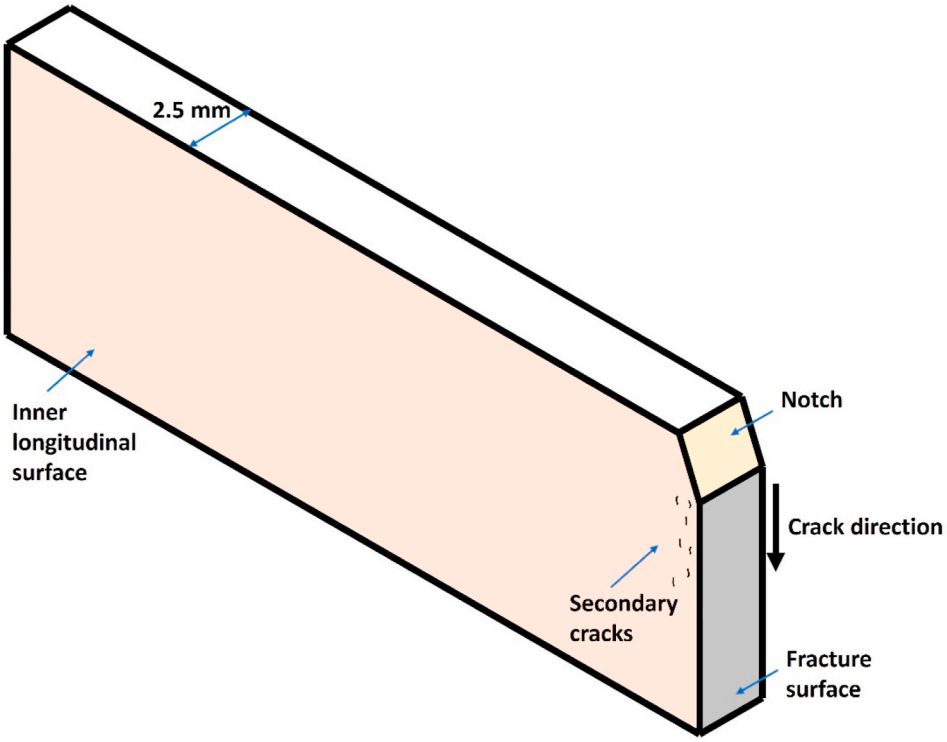

Fig. 11. Subsize CVN specimen longitudinal cut for secondary crack analysis.

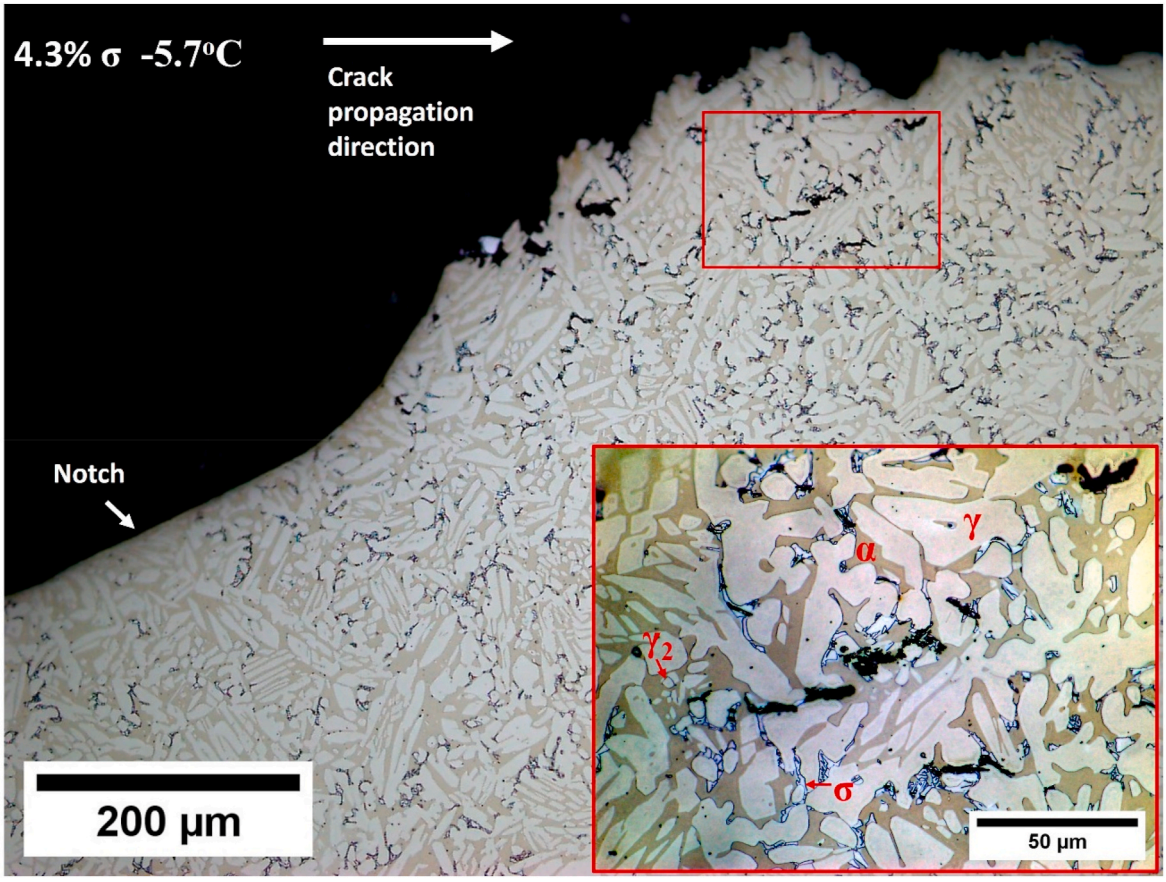

Fig. 12. Inner surface of the specimen with 4.3 % of sigma phase broken at −5.7 °C. The red box detail shows the secondary cracks present in most sigma phase grains. (For interpretation of the references to color in this figure legend, the reader is referred to the Web version of this article.)

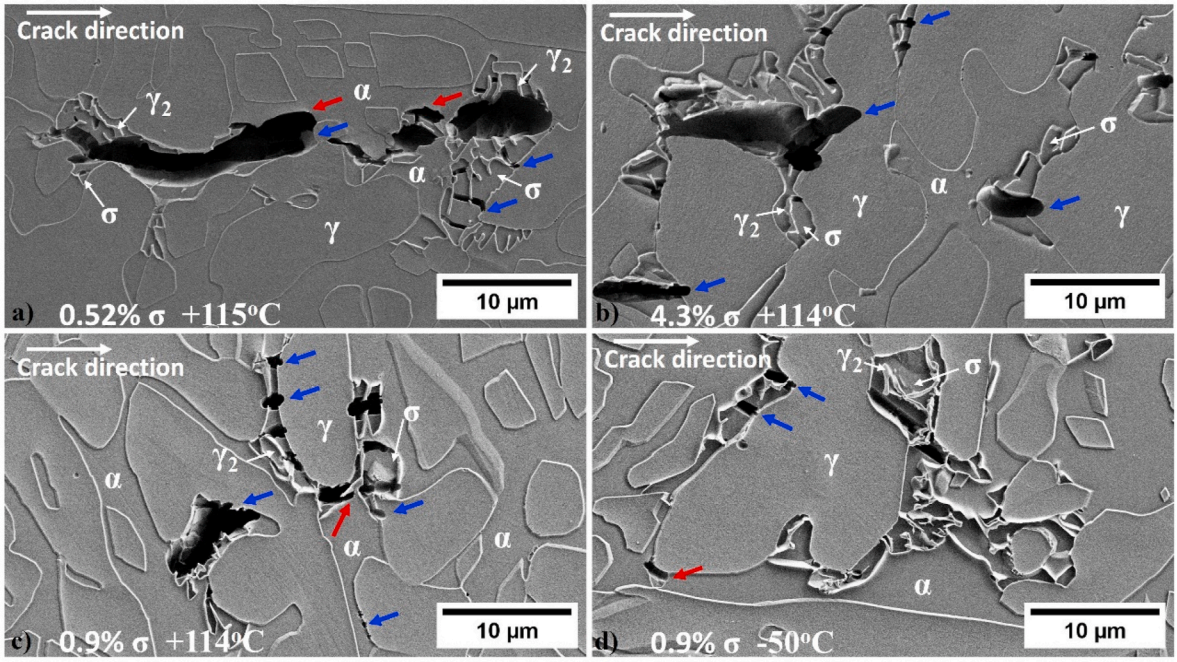

Fig. 13. SE SEM images of the samples with distinct sigma phase volumes and temperature test. The blue arrows indicate the cracks arrested on austenitic grains. Conversely, the red arrow mark cracks arrested on ferritic grains. (For interpretation of the references to color in this figure legend, the reader is referred to the Web version of this article.)

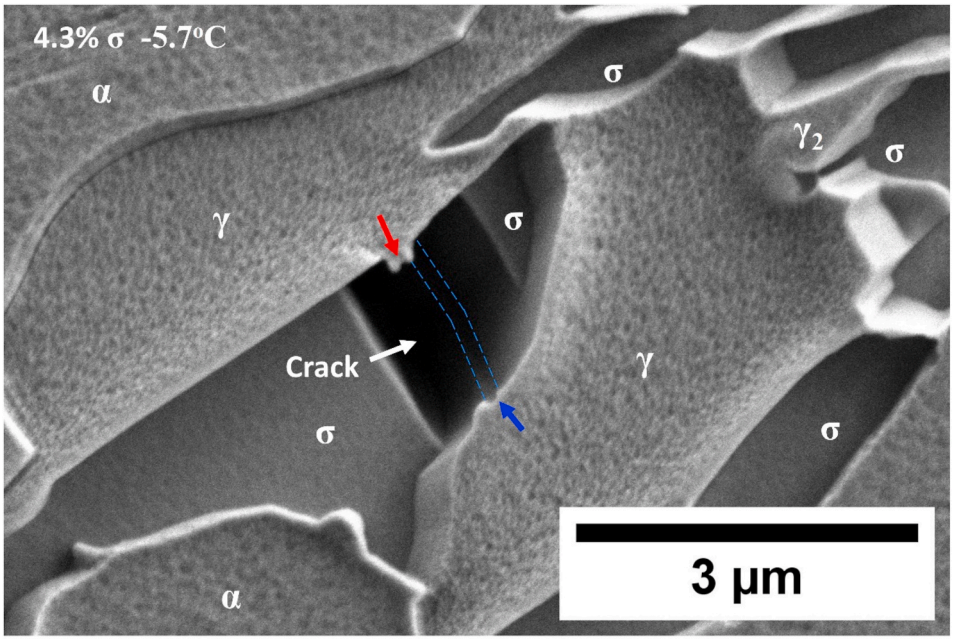

Fig. 14. SE SEM on specimen with 4.3 % σ phase volume broken at −5.7 °C. Detail of a secondary crack through a sigma phase grain suggesting crack deformation on the austenite interface, at the start (red arrow) and stop (blue arrow) regions of the crack. (For interpretation of the references to color in this figure legend, the reader is referred to the Web version of this article.)

Therefore, it is believed that further fracture mechanics analysis might be able to find a critical sigma phase grain size as critical flaw size is used in non-destructive testing (NDT) and engineering critical assessment (ECA).

4. Conclusions

This work presented an evaluation of the impact toughness of HDSS welding metal under different heat inputs and sigma volume fractions induced by thermal-physical simulation. Thus, the following conclusions can be stated:

1. Even small volume of sigma phase such as 0.5 % drastically reduced the maximum ductility, USE, to 50 % of the sigma phase free material.
2. Volume of 0.5 % sigma phase cause the DBTT to increase 26 °C, a high reduction of toughness.

3. Impact toughness (CVN) evaluation showed the condition with 2.0 kJ/mm presented a slightly higher ductile performance due to the higher austenite volume.
4. The subsize CVN testing revealed that the DBTT and USE values can be described through sigmoidal behavior as a function of the sigma phase volume fraction.
5. A sigmoidal regression fitted for the DBTT value as a function of sigma phase volume showed the increase of the DBTT up to an asymptotic behavior at −7 °C.
6. The subsize CVN USE regression denoted an asymptote at 12 J for higher sigma phase volumetric fractions.
7. Secondary crack indicated that the crack propagation is dependent on the sigma phase grain size and orientation.

CRediT authorship contribution statement

Andres Acuna: Writing – review & editing, Writing – original draft, Validation, Methodology, Investigation, Formal analysis, Data curation, Conceptualization. **Kaue Correa Riffel:** Writing – review & editing, Validation, Investigation. **Antonio Ramirez:** Supervision, Resources, Funding acquisition.

Declaration of generative AI and AI-assisted technologies in the writing process

During the preparation of this work the author(s) used ChatGPT 3.5 and Grammarly in order to improve language, and readability. After using this tool/service, the author(s) reviewed and edited the content as needed and take(s) full responsibility for the content of the publication.

Declaration of competing interest

The authors declare that they have no known competing financial interests or personal relationships that could have appeared to influence the work reported in this paper.

Data availability

The data that has been used is confidential.

Acknowledgments

The authors thank the Manufacturing and Materials Joining Innovation Center (Ma2JIC) and NSF (IUCRC program, awards 1539992, 1822144, and 2052747). OSU Center for Electron Microscopy and Analysis (CEMAS) for its support in microscopy. Industry mentors R. Menon, M. Denault, P.Björnstedt, and V. Hosseini for providing the material and fruitful technical discussions.

Appendix A. Supplementary data

Supplementary data to this article can be found online at https://doi.org/10.1016/j.msea.2024.146948.

References

[1] J.O. Nilsson, Super DUPLEX stainless-steels, Mater. Sci. Technol. 8 (8) (Aug 1992) 685–700, https://doi.org/10.1179/mst.1992.8.8.685.
[2] B. Hwang, T.H. Lee, S.J. Park, C.S. Oh, S.J. Kim, Correlation of austenite stability and ductile-to-brittle transition behavior of high-nitrogen 18Cr-10Mn austenitic steels, Materials Science and Engineering a-Structural Materials Properties Microstructure and Processing 528 (24) (Sep 2011) 7257–7266, https://doi.org/10.1016/j.msea.2011.06.025.
[3] M. Knyazeva, M. Pohl, Duplex steels. Part II: Carbides and nitrides (in English), Metallography Microstructure and Analysis 2 (5) (Oct 2013) 343–351, https://doi.org/10.1007/s13632-013-0088-2.
[4] M. Knyazeva, M. Pohl, Duplex steels: Part I: genesis, formation, structure (in English), Metallography Microstructure and Analysis 2 (2) (Apr 2013) 113–121, https://doi.org/10.1007/s13632-013-0066-8.
[5] *RP 582 - Welding Guidelines For the Chemical, Oil, and Gas Industries*, A. P. I. API, 1220 L Street, NW, Washington, DC 20005, 2016.
[6] A. Acuna, A. Ramirez, R. Menon, P.-Å. Björnstedt, L. Carvalho, Developing a weld overlay specification for hyper duplex stainless steel, in: ASME 2021 Pressure Vessels & Piping Conference, 4, 2021 V004T06A042, https://doi.org/10.1115/pvp2021-62042.
[7] A. Acuna, A. Ramirez, K.C. Riffel, Using kinetics to avoid sigma phase formation on hyper duplex stainless weld cladding, Sci. Technol. Weld. Join. (2023-08-29 2023) 1–9, https://doi.org/10.1080/13621718.2023.2246719.
[8] H. Sieurin, Fracture toughness properties of duplex stainless steels. Ph.D., Materials Science and Engineering, Royal Institute of Technology, Stockholm, Sweden, 2006.
[9] H. Sieurin, R. Sandstrom, Fracture toughness of a welded duplex stainless steel, Eng. Fract. Mech. 73 (4) (Mar 2006) 377–390, https://doi.org/10.1016/j.engfracmech.2005.03.009.
[10] E.C. Bain, W.E. Griffiths, An Introduction to the Iron Chromium-Nickel Alloys, 75, Transactions of the American Institute of Mining and Metallurgical Engineers, 1927, pp. 166–211.
[11] M.J. Marcinkowski, D.S. Miller, A study of defect sub-structures in the Fe–Cr sigma phase by means of transmission electron microscopy (in English), Phil. Mag. 7 (78) (1962) 1025–1059, https://doi.org/10.1080/14786436208212898, 1059, 01/01/.
[12] G. Mima, S. Imoto, Changes of Internal Friction and Young's Modulus with Heat-Treatment of an Iron-Chromium Alloy, 2, Technology reports of the Osaka University, 1952, pp. 201–208.
[13] K. Bungardt, W. Spyra, Untersuchungen über die Temperaturabhängigkeit des Elastizitätsmoduls der Eisen-Chrom-Sigmaphase, Arch. für das Eisenhuttenwes. 29 (1958) 471–477.
[14] E23 - Standard Test Methods For Notched Bar Impact Testing Of Metallic Materials, A. S. f. T. a. M.-. ATSM, 2018.
[15] L. E., M. C.N., and S. R.L, "Overview of NIST Activities on Sub-size and Miniaturized Charpy Specimens: Correlations with Full-Size Specimens and Verification Specimens for Small-Scale Pendulum Machines," American Society of Mechanical Engineers, Pressure Vessels and Piping Division doi: 10.1115/PVP2015-45159.
[16] I. Calliari, M. Breda, E. Ramous, K. Brunelli, M. Pizzo, C. Menapace, Impact toughness of an isothermally treated Zeron^{A}®100 SDSS, J. Mater. Eng. Perform. 21 (10) (Oct 2012) 2117–2123, https://doi.org/10.1007/s11665-012-0138-y.
[17] I. Calliari, G. Straffelini, E. Ramous, Investigation of secondary phase effect on 2205 DSS fracture toughness, Mater. Sci. Technol. 26 (1) (Jan 2010) 81–86, https://doi.org/10.1179/174328408x388103.
[18] M. Breda, I. Calliari, E. Ramous, M. Pizzo, L. Corain, G. Straffelini, Ductile-to-brittle transition in a Zeron (R) 100 SDSS in wrought and aged conditions, Materials Science and Engineering a-Structural Materials Properties Microstructure and Processing 585 (Nov 2013) 57–65, https://doi.org/10.1016/j.msea.2013.07.068.
[19] Y. Maehara, M. Koike, N. Fujino, T. Kunitake, Precipitation behavior of σ phase in a duplex phase stainless steel, Tetsu-To-Hagane 67 (3) (1981) 577–586, https://doi.org/10.2355/tetsutohagane1955.67.3_577.
[20] Z.Q. Zhang, H.Y. Jing, L.Y. Xu, Y.D. Han, L. Zhao, Investigation on microstructure evolution and properties of duplex stainless steel joint multi-pass welded by using different methods, Mater. Des. 109 (Nov 2016) 670–685, https://doi.org/10.1016/j.matdes.2016.07.110.
[21] T.H. Wu, J.J. Wang, H.B. Li, Z.H. Jiang, C.M. Liu, H.Y. Zhang, Effect of heat input on austenite microstructural evolution of simulated heat affected zone in 2205 duplex stainless steel, J. Iron Steel Res. Int. 26 (5) (May 2019) 435–441, https://doi.org/10.1007/s42243-018-0134-z.
[22] H. Sieurin, E.M. Westin, M. Liljas, R. Sandstrom, Fracture toughness of welded commercial lean duplex stainless steels, Weld. World 53 (3–4) (Mar-Apr 2009) R24–R33, https://doi.org/10.1007/bf03266700.
[23] Y.Y. Zhang, Z.J. Liu, D.M. Li, Influence of aging temperature on metallurgy, impact toughness and pitting behavior of flux-cored arc welded 2205 duplex stainless steel joint, Mater. Trans. 62 (6) (2021) 756–762, https://doi.org/10.2320/matertrans.MT-M2020331.
[24] S. Topolska, J. Labanowski, IMPACT-TOUGHNESS investigations of duplex stainless steels, Materiali in Tehnologije 49 (4) (Jul-Aug 2015) 481–486.
[25] J.H. Kim, E.J. Oh, B.C. Lee, C.Y. Kang, Effect of aging treatment on impact toughness and corrosion resistance of super duplex stainless steel, J. Mater. Eng. Perform. 25 (1) (Jan 2016) 9–14, https://doi.org/10.1007/s11665-015-1816-3.
[26] F.M. Elsabbagh, R.M. Hamouda, M.A. Taha, On microstructure and microhardness of isothermally aged UNS S32760 and the effect on toughness and corrosion behavior, J. Mater. Eng. Perform. 23 (1) (Jan 2014) 275–284, https://doi.org/10.1007/s11665-013-0619-7.
[27] A. Acuna, A.J. Ramirez, Sigma phase formation kinetics in hyper duplex stainless steel welding filler metal, Mater. Char. 200 (Jun 2023) 112832, https://doi.org/10.1016/j.matchar.2023.112832.
[28] B.B. Zhang, et al., Effect of nitrogen on precipitation behavior of hyper duplex stainless steel S32707, Mater. Char. 175 (May 2021) 111096, https://doi.org/10.1016/j.matchar.2021.111096.
[29] B.B. Zhang, Z.H. Jiang, H.B. Li, S.C. Zhang, H. Feng, H. Li, Precipitation behavior and phase transformation of hyper duplex stainless steel UNS S32707 at nose temperature (in English), Mater. Char. 129 (Jul 2017) 31–39, https://doi.org/10.1016/j.matchar.2017.04.018.
[30] A. Acuna, K.C. Riffel, A. Ramirez, Sigma phase kinetics in DSS filler metals: a comparison of sigma phase formation in the as-welded microstructure of super duplex stainless steel and hyper duplex stainless steel, Mater. Char. (2023), https://doi.org/10.1016/j.matchar.2023.113433.
[31] N.H. Kim, W. Gil, H.D. Lim, C.H. Choi, H.W. Lee, Variation of mechanical properties and corrosion properties with Mo contents of hyper duplex stainless-

steel welds, Met. Mater. Int. 25 (1) (Jan 2019) 193–206, https://doi.org/10.1007/s12540-018-0166-8.
[32] S.M. Kim, J.S. Kim, K.T. Kim, K.T. Park, Y.S. Park, C.S. Lee, Effect of Si and Ce addition on the microstructure and pitting corrosion resistance of hyper-duplex stainless steels, Corrosion 71 (4) (Apr 2015) 470–482, https://doi.org/10.5006/1380.
[33] S.H. Jeon, H.J. Kim, K.H. Kong, Y.S. Park, Effects of copper addition on the passivity and corrosion behavior of 27Cr-7Ni hyper duplex stainless steels in sulfuric acid solution (in English), Mater. Trans. 56 (1) (Jan 2015) 78–84, https://doi.org/10.2320/matertrans.M2014233.
[34] S.H. Jeon, I.J. Park, H.J. Kim, S.T. Kim, Y.K. Lee, Y.S. Park, Effect of Cu on the precipitation of deleterious phases and the mechanical properties of 27Cr-7Ni hyper duplex stainless steels, Mater. Trans. 55 (6) (Jun 2014) 971–977, https://doi.org/10.2320/matertrans.M2013471.
[35] Y.Q. Zhou, X.Y. Cao, S. Mahmood, D.L. Engelberg, A rapid corrosion screening technique for grade 2707 hyper-duplex stainless steel at ambient temperature, Materials and Corrosion-Werkstoffe Und Korrosion 75 (2) (Feb 2024) 227–234, https://doi.org/10.1002/maco.202313943.
[36] S.C. Zhang, et al., Catastrophic oxidation mechanism of hyper duplex stainless steel S32707 at high temperature in air (in English), Mater. Char. 145 (Nov 2018) 233–245, https://doi.org/10.1016/j.matchar.2018.08.041.
[37] J. Wang, W.L. Chen, H.J. Meng, Y.S. Cui, C.L. Zhang, P.D. Han, Influence of sigma phase on corrosion and mechanical properties of 2707 hyper-duplex stainless steel aged for short periods (in English), J. Iron Steel Res. Int. 26 (5) (May 2019) 452–461, https://doi.org/10.1007/s42243-018-0175-3.
[38] L. Sun, et al., Studies on the degree of sensitization of hyper-duplex stainless steel 2707 at 900 degrees C using a modified DL-EPR test, Corrosion Sci. 185 (Jun 2021) 109432, https://doi.org/10.1016/j.corsci.2021.109432.
[39] L. Sun, Y.T. Sun, Y.Y. Liu, N.W. Dai, J. Li, Y.M. Jiang, Effect of annealing temperature on pitting behavior and microstructure evolution of hyper-duplex stainless steel 2707 (in English), Materials and Corrosion-Werkstoffe Und Korrosion 70 (9) (Sep 2019) 1682–1692, https://doi.org/10.1002/maco.201910801.
[40] F. Shang, et al., The microstructure, mechanical properties, and corrosion resistance of UNS S32707 hyper-duplex stainless steel processed by selective laser melting, Metals 9 (9) (Sep 2019) 1012, https://doi.org/10.3390/met9091012.
[41] M. Rajkumar, S.P.K. Babu, T.A. Nagaraj, Intergranular corrosion characteristics of niobium stabilized 27Cr-7Ni-Mo-W-N cast hyper duplex stainless steel (in English), Materials Today-Proceedings, Proceedings Paper 27 (2020) 2551–2555, https://doi.org/10.1016/j.matpr.2019.10.134.
[42] N.P. Raj, K. Sekar, M.A. Joseph, Effect of Temperature on Microstructure Evolution and Localized Corrosion Resistance of High Tungsten Hyper Duplex Stainless Steel, 6, 2019.
[43] H.B. Li, et al., Microbiologically influenced corrosion of 2707 hyper-duplex stainless steel by marine Pseudomonas aeruginosa biofilm, Sci. Rep. 6 (Feb 2016) 20190, https://doi.org/10.1038/srep20190.
[44] D.H. Kim, N.H. Kim, H.W. Lee, Corrosion and cracking characteristics upon aging of hyper duplex stainless steel weld (in English), Mater. Sci. Technol. 36 (7) (May 2020) 783–792, https://doi.org/10.1080/02670836.2020.1743575.
[45] S.M. Kim, J.S. Kim, K.T. Kim, K.-T. Park, C.S. Lee, Effect of Ce addition on secondary phase transformation and mechanical properties of 27Cr–7Ni hyper duplex stainless steels, Mater. Sci. Eng. 573 (2013) 27–36, https://doi.org/10.1016/j.msea.2013.02.044.
[46] S.T. Kim, S.H. Jang, I.S. Lee, Y.S. Park, Effects of solution heat-treatment and nitrogen in shielding gas on the resistance to pitting corrosion of hyper duplex stainless steel welds (in English), Corrosion Sci. 53 (5) (May 2011) 1939–1947, https://doi.org/10.1016/j.corsci.2011.02.013.
[47] A. Keplinger, C. Martinez, M. Hausbauer, M. Kapp, Early stages of deleterious phases in super and hyper duplex stainless steel and their effect on toughness, Frühphasen schädlicher Phasen in Super- und Hyperduplex-Edelstahl und ihr Einfluss auf die Zähigkeit 165 (1) (2020) 33, 01/.
[48] H. Hwang, G. Lee, S. Jeon, Y. Park, Selective dissolution characteristics of 26Cr-7Ni-2.5Mo-3W duplex stainless steel in H2SO4/HCl mixed solution, Mater. Trans. 50 (5) (May 2009) 1214–1218, https://doi.org/10.2320/matertrans.MER2008182.
[49] A.J. Ramirez, J.C. Lippold, S.D. Brandi, The relationship between chromium nitride and secondary austenite precipitation in duplex stainless steels (in English), Metall. Mater. Trans. A 34A (8) (Aug 2003) 1575–1597, https://doi.org/10.1007/s11661-003-0304-9.
[50] E. Lucon, Testing of small-sized specimens, Comprehensive Materials Processing 1 (2014) 135–163, https://doi.org/10.1016/b978-0-08-096532-1.00110-2. Assessing Properties of Conventional and Specialized Materials.
[51] A.J. Ramirez, S.D. Brandi, J.C. Lippold, Secondary austenite and chromium nitride precipitation in simulated heat affected zones of duplex stainless steels, Sci. Technol. Weld. Join. 9 (4) (2004) 301–313, https://doi.org/10.1179/136217104225021715.
[52] *RP 582 - Welding Guidelines For the Chemical, Oil, and Gas Industries*, A. P. I.-. API, 1220 L Street, NW, Washington, DC 20005, 2016.
[53] O.L. Towers, Charpy V-Notch Tests : Influences of Striker Geometry and of Specimen Thickness, Cambridge [England]: The Welding Institute, 1983 (in English).
[54] K. Wallin, New Improved Methodology for Selecting Charpy Toughness Criteria for Thin High Strength Steels, 1994 [Espoo: VTT (in English).
[55] A. Acuna, K.C. Riffel, A. Ramirez, A comparison of sigma phase formation in solubilized hyper duplex stainless steel and super duplex stainless steel filler metals, Metall. Mater. Trans. A 55 (2024) 2881–2896, https://doi.org/10.1007/s11661-024-07442-4.
[56] J.O. Nilsson, P. Kangas, T. Karlsson, A. Wilson, Mechanical properties, microstructural stability and kinetics of sigma-phase formation in 29Cr-6Ni-2Mo-0.38N superduplex stainless steel (in English), Metall. Mater. Trans. A 31 (1) (Jan 2000) 35–45, https://doi.org/10.1007/s11661-000-0050-1.
[57] J.O. Nilsson, A. Wilson, Influence of isothermal phase-transformations on toughness and pitting corrosion of super duplex stainless-steel SAF-2507, Mater. Sci. Technol. 9 (7) (Jul 1993) 545–554, https://doi.org/10.1179/mst.1993.9.7.545.
[58] C.-C. Hsieh, Overview of intermetallic sigma %28%29 phase precipitation in stainless steels, ISRN Metallurgy 2012 (2012) 1–16.
[59] E.O. Hall, S.H. Algie, Sigma phase, J. Inst. Met. 94 (4) (1966), 61-&.
[60] G.J. Mao, C. Cayron, R. Cao, R. Loge, J.H. Chen, The relationship between low-temperature toughness and secondary crack in low-carbon bainitic weld metals, Mater. Char. 145 (Nov 2018) 516–526, https://doi.org/10.1016/j.matchar.2018.09.012.